Front. Chem. Sci. Eng. 2025, 19(12): 115
https://doi.org/10.1007/s11705-025-2588-4

RESEARCH ARTICLE

High CO_2 conversion via plasma assisted reverse water-gas shift reaction over Ag/ZnO catalyst

Chunhong Pan[1,2], Biao Wang (✉)[1,2], Jinman Mao[1,2], Mengjia Li[1,2], Huimin Wang[1,2], Wenyi Chen[1,2], Feng Gao[3], Guoping Hu (✉)[1,2], Xiaolei Fan (✉)[4,5,6], Feng Huang[1,2]

1 School of Rare Earths, University of Science and Technology of China, Hefei 230026, China
2 Key Laboratory of Rare Earths, Ganjiang Innovation Academy, Chinese Academy of Sciences, Ganzhou 341000, China
3 School of Materials, Sun Yat-sen University, Shenzhen 518107, China
4 Department of Chemical Engineering, School of Engineering, University of Manchester, Manchester M139PL, UK
5 Ningbo China Beacons of Excellence Research and Innovation Institute, University of Nottingham Ningbo China, Ningbo 315048, China
6 Wenzhou Key Laboratory of Novel Optoelectronic and Nano Materials, Institute of Wenzhou, Zhejiang University, Wenzhou 325006, China

Abstract Reverse water-gas shift reaction represents a strategic pathway for CO_2 utilization. Despite its potential, reverse water-gas shift reaction via conventional thermal-catalysis faces several challenges, including low equilibrium conversion rates due to thermodynamic constraints, high energy consumption, and insufficient product selectivity. Here, this study demonstrates an evident synergetic effect between plasma and Ag/ZnO, on enhancing reverse water-gas shift reaction. The plasma catalytic system achieved significantly improved performance with a remarkable CO_2 conversion rate of 76.5%, a high CO selectivity of 96.8%, and a CO yield of 74.1%, along with an energy efficiency as high as 0.19 mmol·kJ^{-1}, surpassing the plasma alone system and ZnO catalytic systems. Results from X-ray photoelectron spectroscopy and Auger electron spectroscopy confirm the presence of electronic metal-support interactions between Ag and ZnO, which facilitates the formation of electron-deficient Ag sites and partially reduced ZnO_x species. These reactive sites, along with oxygen vacancies created during reduction treatment, enhance the adsorption and activation of H_2 and CO_2, offering a dominant plasma-assisted surface reaction pathway for the improved reverse water-gas shift reaction. These findings underscore the crucial role of electronic metal-support interactions in manipulating surface environments to facilitate efficient plasma-assisted catalytic reactions, with significant implications for the rational design of catalysts capable of converting CO_2 efficiently under mild conditions.

Received May 8, 2025; accepted May 18, 2025; online July 16, 2025

E-mails: biaowang@gia.cas.cn (Wang B.),
gphu@gia.cas.cn (Hu G.),
xiaolei.fan@manchester.ac.uk (Fan X.)

Keywords non-thermal plasma catalysis, CO_2 conversion, reverse water-gas shift reaction, Ag/ZnO, electronic metal-support interactions

1 Introduction

In recent years, the continuous increase in CO_2 concentration has led to an increasingly severe greenhouse effect and extreme climate problems [1]. To mitigate these environmental challenges, it is imperative to develop effective strategies for reducing atmospheric CO_2 levels. Researchers have focused on innovative strategies for CO_2 management [2]. Specifically, capturing CO_2 and subsequently converting it into high-value-added fuels and chemicals has been acknowledged as the promising solutions [3,4].

One of the attractive methods is the hydrogenation of CO_2 to CO, also known as the reverse water gas shift reaction (RWGS, Eq. (1)). This process can serve as an intermediate step or/and provide CO precursor in the further synthesis of more complex hydrocarbon fuels and platform chemical through Fischer-Tropsch synthesis or other process [5,6]. However, given the inert nature of CO_2 and the thermodynamic equilibrium constraints of RWGS, hydrogenation of CO_2 to CO through traditional thermal conversion methods necessitates high temperatures and the utilization of effective catalysts to achieve an optimal balance between CO_2 conversion and CO selectivity. The inefficiency of heat utilization in conventional reactors further exacerbates the energy-intensive nature of the RWGS process, as only a portion of the applied thermal energy is effectively utilized for CO_2

activation [7]. Additionally, the elevated temperatures required for the reaction negatively impact the performance of metal-based catalysts, particularly non-noble metal catalysts, often leading to sintering or phase segregation [8]. While numerous efforts have been made to optimize the RWGS process at lower temperatures to address these challenges, low-temperature conditions favor undesired competitive reactions such as CO_2 and CO methanation [9]. These competing processes reduce CO selectivity and increase costs associated with product separation. Given these limitations, the advancement of novel catalytic conversion technologies and the development of high-efficiency synergistic catalysts are essential for addressing the energy consumption, efficiency, and selectivity challenges inherent to RWGS reactions.

$$CO_2 + H_2 = CO + H_2O$$
$$\Delta H = 41.17\ \text{kJ}\cdot\text{mol}^{-1}. \quad (1)$$

Recently, CO_2 hydrogenation driven by non-thermal plasma (NTP) has garnered increasing attention as a promising alternative to highly energy-intensive thermocatalytic pathways [10,11]. Owing to its non-equilibrium properties, energetic electrons with a mean energy ranging from 1 to 10 eV can be generated during the NTP process, efficiently activating the reactant gases (i.e., CO_2 and H_2) into reactive species (i.e., free radicals, ions, excited atoms, and molecules) [4,12,13], while maintaining a relatively low temperature across bulk gas and entire reactor. This capability enables the initiation of thermodynamically unfavorable RWGS reactions under near-ambient conditions, thereby significantly reducing capital costs associated with the demand for high temperature-pressure apparatus and operational sites. Additionally, compared with the long-term stability requirements of thermocatalytic processes for energy supply, the ability to rapidly ignite reactions enables instant start-stop control of the NTP process, offering the flexibility to integrate with intermittent and fluctuating renewable energy sources [14].

However, when the NTP process is used in isolation for CO_2 hydrogenation, the conversion of CO_2 and energy efficiency are constrained [15]. The integration of plasma technology with heterogeneous catalysis, also known as plasma catalysis [16], has emerged as a promising strategy to address these challenges. For example, Liu et al. [17] reported an enhanced effect of plasma on the RWGS reaction over Ni-based perovskite catalysts. The formation of uniform Ni-Fe alloy and oxygen vacancies (Ov) over the $La_{0.9}Sr_{0.1}Ni_{0.5}Fe_{0.5}O_{3+\delta}$ catalyst facilitates the dissociation of CO_2 and H_2, resulting in a high CO_2 conversion rate of 60% but with moderate CO selectivity (90%). Sun et al. [18] achieved an increase in CO_2 conversion from 21.3% to 36.7% over Pd/ZnO under plasma conditions, with 96.6% CO selectivity and an energy efficiency of 0.13 $\text{mmol}\cdot\text{kJ}^{-1}$. The improved performance is attributed to the hydrogenation of adsorbed surface CO_2 on Pd/ZnO, which is more effective than gas-phase plasma reaction routes [19]. These studies highlight the importance of suitable catalysts in steering the evolution of plasma-activated species and providing efficient surface reaction pathways. Despite these advancements, designing new plasma-catalyst combinations that minimize side reactions while balancing CO_2 conversion with energy efficiency remains a formidable challenge worthy of further investigation.

Ag-based materials have emerged as promising selective hydrogenation catalysts for the preliminary hydrogenation of C–O/C=O bonds (e.g., regioselective hydrogenation of diethyl oxalate into methyl glycolate) [20]. Furthermore, Ag stands out as one of the few monometallic electrocatalysts capable of achieving CO selectivity approaching 100% in electrocatalytic CO_2 reduction, owing to its weak CO binding affinity [21]. It is noteworthy that Ag also functions as a key promoter in multimetallic catalysts, enabling enhanced catalytic activity through modulation of the electronic structure and optimization of the dispersion of active sites. For example, Mori et al. [22] developed a TiO_2-supported PdAg catalyst featuring isolated, electron-enriched Pd atoms by alloying with Ag, significantly enhancing the hydrogenation of CO_2 into formic acid. However, monometallic Ag has received less attention as a primary catalytic active phase for CO_2 hydrogenation because of its limited capacity for hydrogen dissociation, which was attributed to its completely filled d-band structure [23]. Recent computational and experimental studies have demonstrated that the activation of H_2 can be significantly enhanced on supported Ag due to the formation of various Ag-O interactions [24]. These interactions modulate the electronic and interfacial properties of Ag, resulting in an increased affinity for hydrogen. For instance, Sun et al. [25] studied the hydrogenation of CO_2 to methanol using Ag/In_2O_3 catalysts, achieving 100% methanol selectivity. The excellent catalytic performance can be attributed to the strong interaction between Ag and the support In_2O_3. This interaction places Ag in a positively charged state and increases the availability of interfacial Ov sites, both of which collectively enhance the activation of H_2 and CO_2 [26,27]. The short review above on the relevant state-of-the-arts suggests Ag-based catalysts are promising in promoting CO_2 hydrogenation reactions due to the relatively low cost, stable chemical state, and the flexibility in tuning their electronic and interfacial properties, which can be optimized through the selection of appropriate supports [3].

In this paper, we investigate the catalytic behavior of Ag supported on ZnO catalyst (Ag/ZnO) for plasma-assisted RWGS reaction within a tabular dielectric barrier discharge (DBD) reactor. ZnO was chosen as a support due to its reducibility and abundance of basic sites, which not only enables the modulation and stabilization of Ag's

electronic properties but also offers distinct benefits in the adsorption and activation of CO_2. The Ag/ZnO catalyst, synthesized via a co-precipitation method, exhibited exceptional performance in the plasma-assisted RWGS reaction. It achieved a CO_2 conversion rate of 76.5% and a CO selectivity of 96.8%, in addition to an energy efficiency of 0.19 mmol·kJ^{-1}. Comparative experiments and a variety of characterization techniques were employed to gain insight into the relationship between the electronic metal-support interaction (EMSI) over Ag/ZnO and its pronounced synergistic effect with plasma on CO_2 hydrogenation.

2 Experimental

2.1 Preparation of catalysts

Ag/ZnO catalysts with different Ag contents (2, 5, 10, 15, and 20 wt %) were prepared by the co-precipitation method. To prepare 5% Ag/ZnO, $AgNO_3$ (0.54 g, 99.0 wt % Ag, Aladdin) and $Zn(NO_3)_2{\cdot}6H_2O$ (14.6 g, Aladdin) were dissolved in ultrapure water (80 mL) to form the precursor solution. Subsequently, this precursor solution was added simultaneously with a mixture of precipitators Na_2CO_3 (0.25 mol·L^{-1}) and NaOH (0.25 mol·L^{-1}) into a beaker containing 100 mL of ultrapure water. The beaker was placed in a 60 °C constant temperature water bath under vigorous stirring, and the pH of the reaction was adjusted using the precipitants to maintain the pH of the precursor solution at 9.0–9.5. The resulting solution was continuously stirred in a 60 °C constant temperature water bath for 4 h and separated by centrifugation. The obtained samples were dried in an oven at 90 °C for 10 h and then calcined in a muffle furnace at 370 °C for 4.5 h. Ag/ZnO catalysts with different Ag contents (2, 10, 15, and 20 wt %) were synthesized using the same procedure, and ZnO was also prepared in the same manner without adding $AgNO_3$ to the precursor solution. Ag-based catalysts supported on various materials (CeO_2, SiO_2, and γ-Al_2O_3) were synthesized using the immersion method. Specifically, 3.2 g of CeO_2, 7.5 g of SiO_2, and 4.4 g of γ-Al_2O_3 were separately placed in containers. Equal volumes of $AgNO_3$ precursor solutions were added to each carrier. The mixtures were then stirred thoroughly and left to stand at room temperature for 24 h. Subsequently, the samples were dried at 90 °C in an oven for 10 h and subsequently calcined for further use. Before catalytic testing at NTP, the obtained catalyst samples were thoroughly ground and placed in a tubular furnace under H_2/Ar (H_2/Ar = 1:9, 20 mL·min^{-1}) mixed atmosphere at 370 °C for reduction for 4 h. The Ag/ZnO and ZnO were then pressed into thin wafers (2 mm × 2 mm, thickness ~0.4 mm) and sieved to 20–40 mesh.

2.2 Characterization methods

Field emission scanning electron microscopy (SEM, JEOL, Japan) meticulously characterizes the surface morphology of solid samples. X-ray diffraction (XRD) is performed by a Bruker X-ray diffractometer (D8 Advance) using a Cu Kα radiation source with the tube voltage and current being 40 kV and 40 mA, respectively, alongside a wavelength of 0.15418 nm. The diffraction patterns were recorded using a step size of 0.02° in a 2θ range of 10°–90°. Images of transmission electron microscope (TEM) and a high-resolution TEM (HR-TEM) are shot on a Talos F200C with a CCD camera from FEI. Laboratory$_6$, which was used as the filament, and the accelerating voltage constant of 200 kV. The model of laser Raman spectrometer used in this experiment is HORIBA LabRAM HR Evolution, which adopts a 532 nm laser light source, experimental power of 50 mW, 1800 gr·mm^{-1} grating, and a 50 times Leica long focal length objective lens. The scanning range is 200–900 cm^{-1}, and the test intensity is 10%. X-ray photoelectron spectroscopy (XPS) is performed on a Thermo Scientific Kα XPS system. The excitation source is Al Kα rays with the energy of 1486.6 eV, using C 1s peak at 284.8 eV to reference the binding energies. Auger electron spectroscopy (AES) is performed on ESCALAB 250xi XPS system. Test conditions: vacuum degree of 1 × 10^{-8}, non-monochromatic Al Kα (photon energy of 1486.6 eV) anode target; scanning range of binding energy (BE) of 0~1000 eV, pass energy of 40 eV, and scanning step length of 0.1 eV·step^{-1}. Pore size data of catalysts were calculated by the Barret-Joyner-Halenda method. These data are obtained by N_2 isotherm adsorption and desorption test on an ASAP2460 physical adsorption instrument made by Micromeritics. The sample is degassed under vacuum at 300 °C for 4 h, and the relative pressure range of P/P_0 = 0–1.0 during the test. The adsorption and activation of H_2-temperature programmed desorption (H_2-TPD) and CO_2-TPD on different surfaces (ZnO or Ag/ZnO) are studied on Micromeritics Autochem II 2920 chemisorption instrument. In a typical TPD analysis, the reactants (H_2 and CO_2) are adsorbed on the surface (ZnO or Ag/ZnO), and the desorption process is carried out by increasing the temperature in the absence of plasma. The Ov of the catalyst is further measured by Bruker electron paramagnetic resonance (EPR) spectrometer EMX plus-6/1, and O_2 is first pre-adsorbed at room temperature, and then detected at a liquid nitrogen temperature of 77 K.

2.3 Experimental setup and plasma-catalytic tests

The NTP catalytic CO_2 hydrogenation is performed in a DBD reactor. The catalysts are placed in a tube furnace and reduced by H_2/Ar mixed gas (H_2/Ar = 1:9) at 370 °C for 4 h before the reaction. We measured the applied

voltage using a Tektronix high-voltage probe (P6015A) and the current with a Tektronix current monitor (TCP0030). The voltage on the external capacitor was sampled using a Tektronix P6139B probe. All of the electrical signals were recorded using an oscilloscope (Tektronix DPO 3034). The plasma power was determined using the typical Lissajous figure approach.

During the specific experiment, 0.16 g of catalysts (with an average particle size of 20–40 mesh) was filled in the discharge area, with a length of about 40 mm and first purged by Ar (20 mL·min^{-1}) for 15 min, and then pre-treated *in situ* by gas discharge using H_2 (20 mL·min^{-1}) for 30 min at the peak voltage of 15.8 kV and frequency of 7.5 kHz. After the pretreatment, H_2/CO_2 mixed gas (H_2/CO_2 = 3:1, 20 mL·min^{-1}) as the reaction gas, and the detailed process and principle of the reaction through DBD plasma co-catalyst discharge are shown in Fig. S1 (cf. Electronic Supplementary Material, ESM). During the experiment, the plasma reaction was maintained at a constant temperature of 25 °C and ambient pressure, and periodic sampling of the reactor was performed to analyze the gas composition of the outlet flow using an online gas chromatograph (SHIMADZU GC2014C). After the gas outflow, the liquid phase product is condensed by the cold trap device (before gas chromatography analysis), and the gas phase product is fully entered into the gas chromatography. The average velocity of the dry gas flow rate of the inlet and outlet stream from the reactor was measured by a soap bubble flow meter.

The definition and calculation of key reaction properties such as CO_2 conversion, CO selectivity, and yield of the sample, and energy consumption of the product generation are determined by Eqs. (2–6). Carbon balances of the experiments here were estimated at 96%–99%. In the reaction, the conversion of CO_2 is defined as:

$$X_{H_2}(\%) = \frac{H_2 \text{ converted (mol)}}{H_2 \text{ input (mol)}} \times 100. \quad (2)$$

The conversion of H_2 is defined as:

$$X_{H_2}(\%) = \frac{H_2 \text{ converted (mol)}}{H_2 \text{ input (mol)}} \times 100. \quad (3)$$

The selectivity of CO is calculated as:

$$S_{CO}(\%) = \frac{CO \text{ produced (mol)}}{CO_2 \text{ converted (mol)}} \times 100. \quad (4)$$

The CO yield is defined as:

$$Y_{CO}(\%) = X_{CO_2} \times S_{CO} \times 100. \quad (5)$$

The energy efficiency for CO production is calculated as:

$$EE_{CO}\ (\text{mmol}\cdot\text{kJ}^{-1}) = \frac{CO \text{ produced (mol}\cdot\text{s}^{-1})}{\text{Power (W)}}. \quad (6)$$

In the equation, EE_{CO} (mmol·kJ^{-1}) represents the energy efficiency of CO production, and the discharge power was calculated using the Lissajous curve method (Fig. S2, cf. ESM). The discharge power is 25.31 ± 0.2 W under the optimal catalytic performance at an applied voltage of 28 kV in this work.

3 Results and discussion

3.1 Characterization of the materials/catalysts

We conducted experiments for knowing the effect of Ag loading on plasma-assisted RWGS, and 5 wt % Ag loading (5% Ag/ZnO) was optimum (to be discussed later), hence the relevant comparative study and characterization were conducted using 5% Ag/ZnO. Figure 1(a) displays the XRD patterns of the as-prepared (calcined) and reduced Ag/ZnO samples. Both exhibit distinct diffraction peaks corresponding to wurtzite ZnO (JCPDS 04-003-2106) and metallic Ag (JCPDS 01-071-6549) [28], with no extraneous peaks present, indicating the successful fabrication of ZnO-supported Ag. The formation of metallic silver results from the decomposition of Ag_2O precursor (i.e., $2Ag_2O \rightarrow 4Ag + O_2$), which occurs during the high-temperature calcination process for sample fabrication. Apart from a minor intensification of the diffraction peak corresponding to metallic Ag, the XRD pattern of the reduced Ag/ZnO showed no other notable differences compared to that of calcined Ag/ZnO. This indicates that the Ag_2O underwent further decomposition to produce Ag during the reduction process, with the ZnO component remaining unaffected and stable. The morphological characteristics of Ag/ZnO were examined using SEM (Fig. S3, cf. ESM), both as-prepared and reduced Ag/ZnO present an irregular granular morphology with a non-uniform particle size distribution, and it demonstrates a highly aggregated, porous macroscopic surface structure.

The specific surface area and pore size distribution were obtained via nitrogen adsorption/desorption isotherms (Fig. S4 and Table S1, cf. ESM). The specific surface area of Ag/ZnO after thermal reduction were measured to drop slightly (from 17 to 14 m·g^{-1}), likely due to slight agglomeration of Ag/ZnO during the thermal reduction. To gain additional insights into the changes in physical property of materials during catalyst fabrication processes, the as-prepared ZnO, Ag/ZnO, and reduced ZnO were characterized using Raman spectroscopy. As shown in Fig. 1(b), both as-prepared ZnO and Ag/ZnO exhibited distinct signatures of hexagonal ZnO (Fig. 1(b)), evident from the characteristic phonon frequencies observed at approximately 332, 380, and 437 cm^{-1}. Additionally, a pronounced shoulder at 574 cm^{-1}, assigned to the longitudinal optical phonon mode (i.e., E1(LO)) of hexagonal ZnO, appears on the Raman

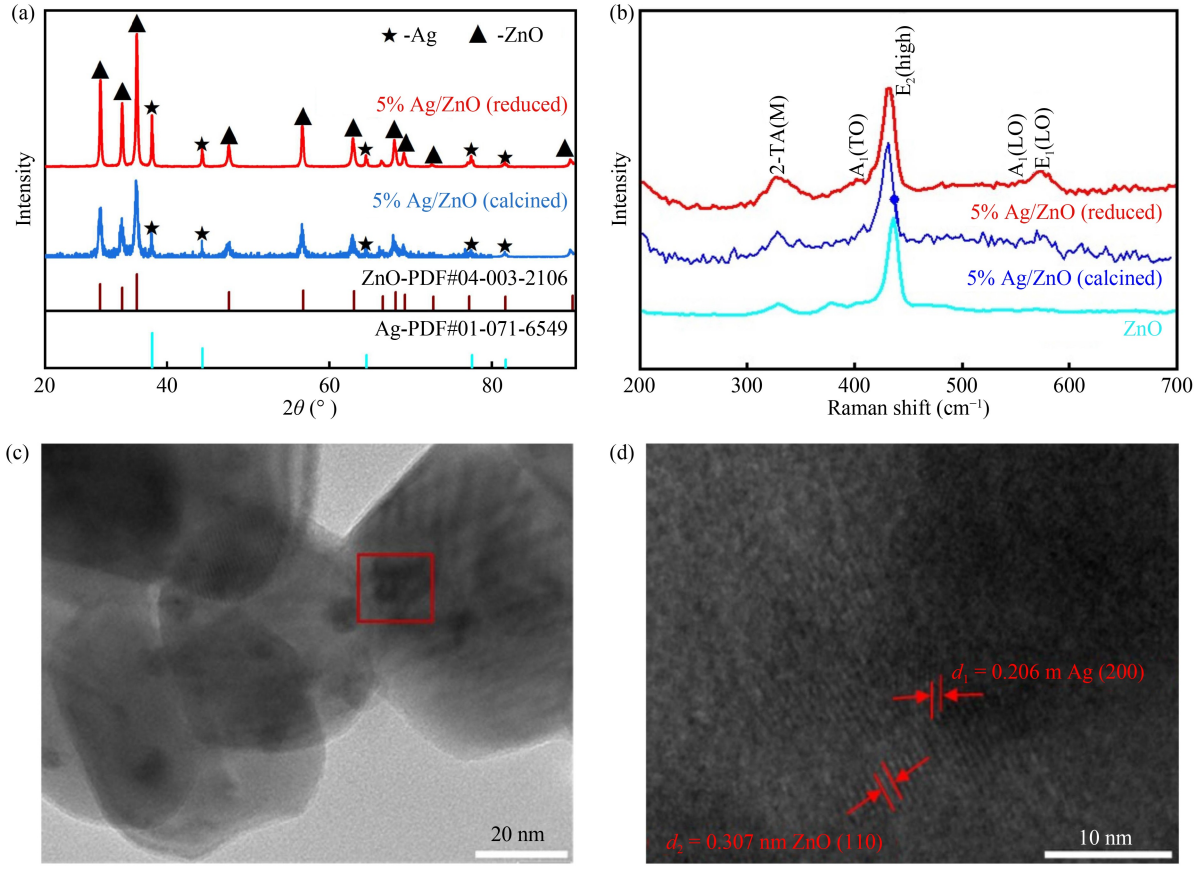

Fig. 1 (a) XRD and (b) Raman spectra of the catalysts; (c) TEM and (d) HR-TEM image of the reduced Ag/ZnO catalyst.

spectra of the reduced Ag/ZnO [29]. The E1(LO) phonon mode is commonly associated with oxygen deficiency in ZnO, indicating the formation of Ov on Ag/ZnO following hydrogen reduction treatment. TEM images are presented in Figs. 1(c) and 1(d) to illustrate the detailed structure of the reduced Ag/ZnO showing the distribution of Ag nanoparticles with an average size of roughly 10 nm (spherical black dots on the ZnO substrate). HR-TEM (Fig. 1(d)) reveals that Ag and ZnO are tightly interconnected, displaying lattice spacings of 0.307 and 0.206 nm, respectively, which correspond to the (110) plane of ZnO and the (200) planes of Ag [30].

AES and XPS were utilized to investigate the electronic properties of Ag/ZnO, aiming to further elucidate the interaction between silver species (Ag^0 and Ag^+) and ZnO. As shown in Fig. 2(a), Zn LMM Auger spectra resolve Zn^{2+} (985–988 eV) and its reduced state (the shoulder peak in the range of 992–995 eV), such as metallic Zn or partially reduced ZnO_x [29]. This shoulder peak, approximately at 992.1 eV, becomes prominent after treatment with H_2 reduction. Concurrently, the Zn LMM peak shifts toward higher kinetic energy, suggesting an increase in charge density at the Zn sites following the reduction treatment. Figure 2(b) presents the Ag 3d XPS spectra for as-prepared Ag/ZnO. The Ag $3d_{3/2}$ peaks can be deconvoluted into two distinct peaks at 373.4 and 372.6 eV, corresponding to oxidized Ag (Ag^+) and metallic Ag (Ag^0) states, respectively [31]. Noteworthy is the deviation in BE shift between Ag^+ and Ag^0 from expectations based on electronegativity arguments, which typically associate higher charge density with a more negative BE. The anomaly arises because the core-level BE shifts in Ag are significantly influenced by multiple factors, including lattice potential, work function changes, and extra atomic relaxation energy, rather than being primarily determined by the difference in electronegativity, as is often the case for other elements [31]. Reduced Ag/ZnO displays similar XPS signals. However, variations in the area and position of each component peak are observed. Specifically, the intensity of the Ag^+ peak in reduced Ag/ZnO decreases from 35.7% to 22.2%, indicating that a portion of Ag^+ was preserved under a hydrogen reduction environment. The stable persistence of oxidized Ag under reductive conditions can be attributed to the vicinity of Ov adjacent to Ag sites and the interaction between Ag and ZnO, which will be discussed later. The presence of oxidized Ag alongside Ag^0 on the support material greatly benefits the concurrent activation of both H_2 and CO_2. It has been found that the hydrogen absorption and splitting process occurs readily on electron-deficient Ag species [32,33], including supported silver ions and oxidized silver surfaces. Conversely, metallic Ag and/or negatively charged Ag sites enhance CO_2 adsorption and activation

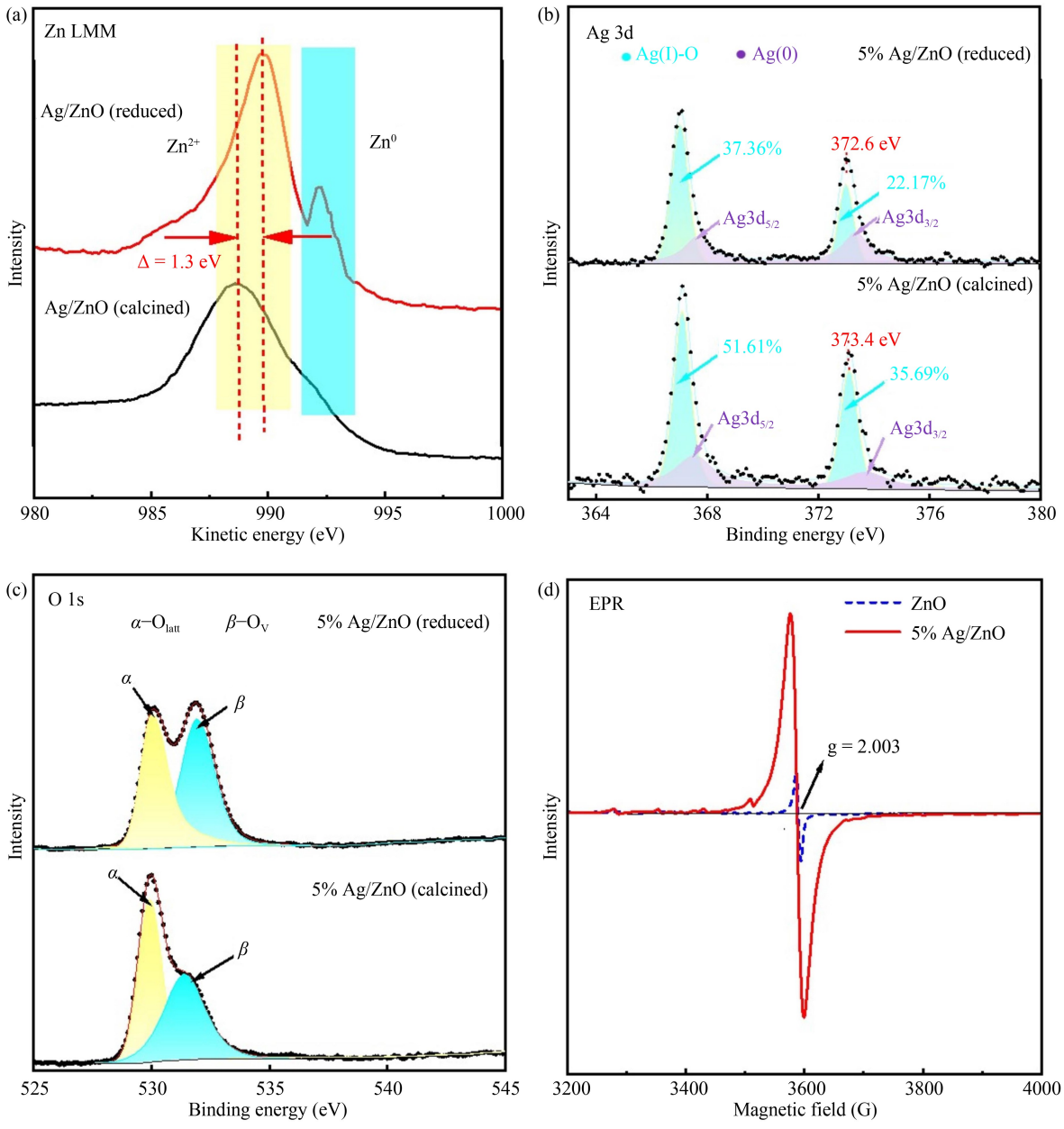

Fig. 2 (a) Zn LMM AES spectra, (b) Ag 3d, and (c) O 1s XPS spectra of the as-prepared Ag/ZnO and reduced Ag/ZnO; (d) EPR spectra of the reduced Ag/ZnO at 77 K.

[33], promoting the selective formation of CO products due to their moderate CO adsorption energy [34]. Furthermore, beyond altering the Ag^0/Ag^+ ratio, a significant shift of the Ag $3d_{5/2}$ peak toward a lower BE of approximately 0.8 eV was observed on the reduced Ag/ZnO, suggesting an attenuation of electron density at Ag sites [35]. The opposite changes in electron density confirm charge transfer at the interface between supported Ag and ZnO, a phenomenon typically attributed to the formation of EMSI [36]. Figure 2(c) illustrates the O 1s spectra of Ag/ZnO before and after reduction, where two peaks corresponding to lattice oxygen (at 530.5 eV) and Ov (at 531.6 eV) can be distinguished [37]. The relative concentration changes of Ov can be determined by analyzing the peak area variations of the O 1s signals.

As shown in Table 1, in comparison to the as-prepared Ag/ZnO catalyst, the proportion of the peak associated with Ov in the reduced Ag/ZnO increased from 29.2% to 53.5%, suggesting that reduction resulted in the formation of additional Ov. The abundance of Ov defects on reduced Ag/ZnO can be additionally substantiated by EPR results, revealing more robust resonances at g values of 2.003, indicative of unpaired electrons lodged in Ov. Ov on ZnO have been recognized as important sites for the dissociation of CO_2 and C–O bond cleavage, facilitating the efficient CO_2 hydrogenation to desired products [38]. Additionally, Ov is located at the interface

Table 1 O 1s date of calcined (cal) and reduced (red) Ag/ZnO

Sample	*α*		*β*	
	B.E.a (eV)	Content (%)	B.E.a (eV)	Content (%)
5%Ag/ZnO (cal)	530.3	70.8	531.5	29.2
5%Ag/ZnO (red)	530.1	46.5	531.9	53.5

of supported Ag species, and the support was verified to stabilize the thermodynamically unstable oxidized Ag species (i.e., Ag^+) under the reductive conditions of a hydrogenation reaction [39].

H_2-TPD and CO_2-TPD were carried out to investigate the chemisorption and activation of H_2 and CO_2 over the reduced ZnO and Ag/ZnO (Fig. 3 and Table 2). Figure 3(a) depicts three types of H_2 desorption peaks within its feature temperature zone. The desorption peaks observed at temperatures below 150 °C are generally ascribed to the weak desorption of H_2 molecules that are physically adsorbed on the catalyst's surface [40]. The peaks situated between 150 and 300 °C can be attributed to the adsorption of free hydrogen atoms on Ag and ZnO, as well as their interfaces. Peaks occurring above 300 °C are linked to the irreversible desorption of hydrogen that has spilled over from the ZnO surface [41]. When contrasted with pure ZnO, Ag/ZnO displays two new desorption peaks at 154 and 236 °C, signifying the existence of H_2 spillover from the Ag site to ZnO_x, which is vital for the hydrogenation of CO_2 adsorbed on the Ag/ZnO surface [42]. Upon loading with Ag, the intensity of all desorption peaks increases, exhibiting a 3.4-fold increase in hydrogen desorption from Ag/ZnO compared to pure ZnO (i.e., 0.567 *vs*. 0.162, see Table 2).

The enhanced ability of Ag/ZnO to adsorb and decompose H_2 molecules is likely due to the electron-poor Ag species that emerge from electron transfer from supported Ag to ZnO and are stabilized by Ov at the interface. Figure 3(b) illustrates the CO_2-TPD profiles of Ag/ZnO and ZnO, presenting three main desorption zones. These zones are characterized as weak (< 200 °C), medium (200–400 °C), and strong (> 400 °C) basic sites. Compared with ZnO, Ag/ZnO exhibits a new CO_2 desorption peak at 189 °C, which is attributed to carbonates adsorbed on the Ag sites [43,44]. The desorption peak intensity for Ag/ZnO within the 200–400 °C temperature range is elevated, rising from 0.5 to 0.8, which signifies that the addition of Ag results in the emergence of additional medium-strength acid sites [45]. Simultaneously, the desorption peak of bidentate carbonates bound to these medium-strength acid sites was observed at a higher temperature of 326 °C, indicating a stronger interaction between CO_2 and the catalysts. This robust interaction, crucial for dissociative adsorption and selective conversion of CO_2, may be attributed to the formation of coordinatively unsaturated metal sites (i.e., ZnO_x) and Ov on Ag/ZnO [46]. TPD results demonstrate that Ag/ZnO is considerably more advantageous for activating H_2 and CO_2 than ZnO.

3.2 Plasma-assisted RWGS

The performance of plasma-assisted CO_2 hydrogenation reactions in the plasma alone, plasma + ZnO, and plasma + Ag/ZnO systems was compared in Fig. 4(a). In the plasma alone system, the CO_2 conversion is rather limited at 21.8%, which was mainly due to the plasma-induced CO_2 dissociation in the gas phase. The resulting CO selectivity is 92.6%, with a corresponding CO yield of 20.2%. The result is consistent with that of previous studies [17,19]. In the plasma gas phase reaction process (Fig. S5, cf. ESM), the high-energy electrons produced during the high-voltage discharge process can directly induce the dissociation of CO_2 to generate CO*, which

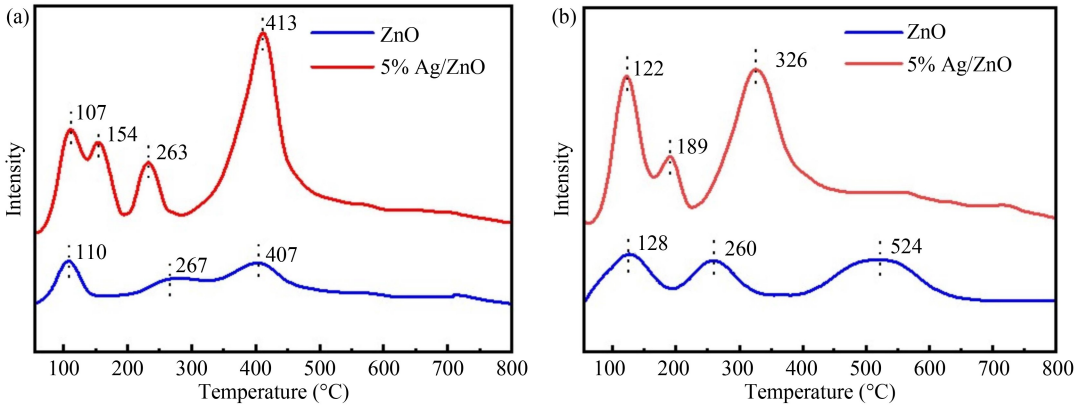

Fig. 3 (a) H_2-TPD, and (b) CO_2-TPD of the reduced ZnO and reduced Ag/ZnO.

Table 2 Total H_2 and CO_2 adsorption amount on the catalysts under investigation

Catalysts	Total H_2 adsorption (mmol·g_{cat}^{-1})	Total CO_2 adsorption (mmol·g_{cat}^{-1})
ZnO	0.164	0.276
5%Ag/ZnO	0.567	0.586

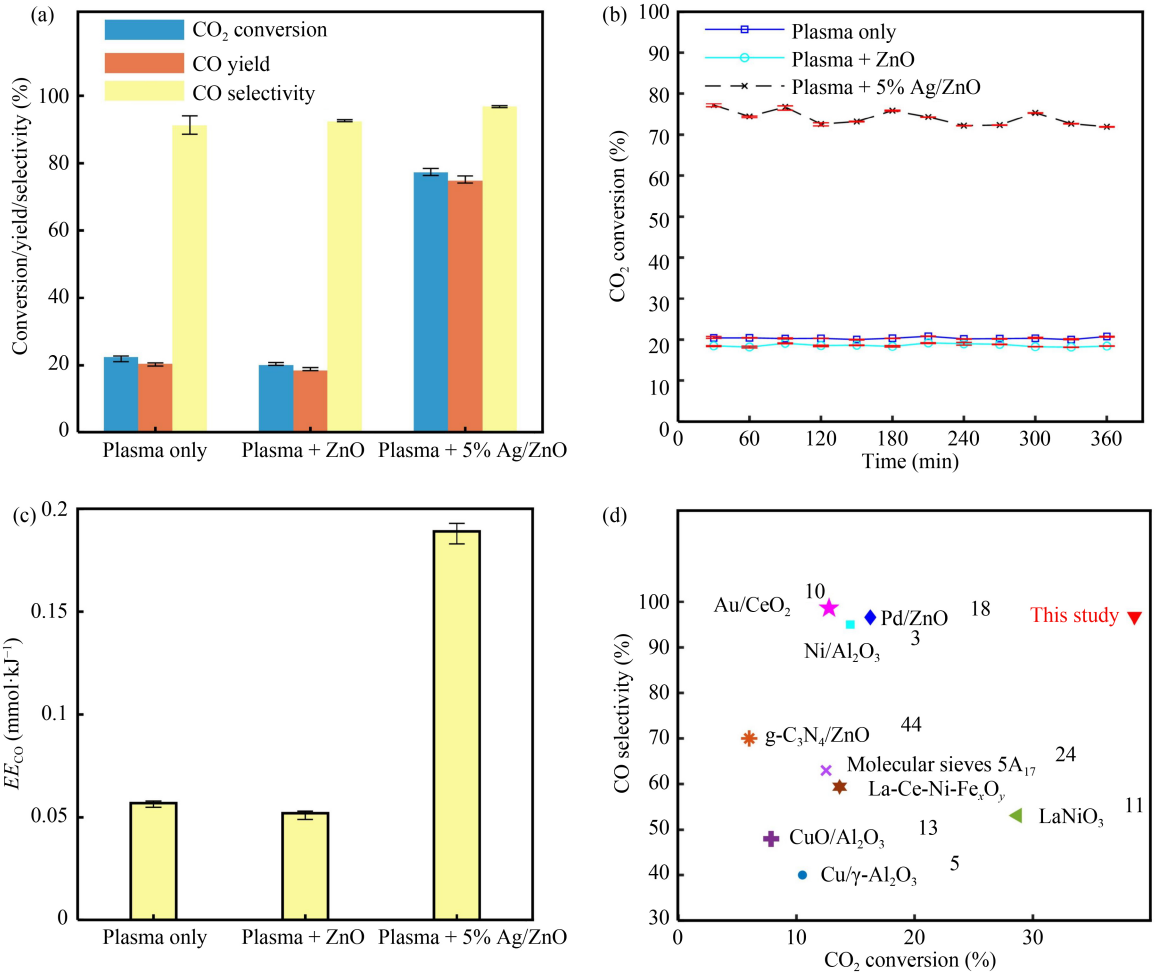

Fig. 4 (a) Performance of RWGS in different plasma systems, (b) stability test, and (c) energy efficiency based on CO production in different plasma systems (H_2/CO_2 = 3:1, total flow = 20 mL·min^{-1}, applied peak voltage of 28 ± 0.2 kV, frequency of 7.5 kHz, discharge power of 25.31 ± 0.2 W), and (d) comparison of performance on RWGS reactions driven by plasma of different materials/catalysts.

could quench to give CO. In addition, and H_2 dissociation occurs as well in gas discharge producing highly reactive hydrogen radicals, which could react with CO_2 to form CO (RWGS). The inclusion of ZnO in the discharge gap of the DBD reactor did not improve the performance of CO_2 hydrogenation, in fact, the conversion of CO_2 experienced a slight decrease (from 21.8% to 20.3%), which is consistent with the findings reported by Sun et al. [18]. The presence of ZnO diminished the occurrence of filamentary discharges, which in turn decreased the production of reactive species essential for gas-phase reactions [47]. On the other hand, ZnO is not a catalyst for enabling RWGS in thermal systems, hence not expecting ZnO could promote the surface reactions under the plasma condition.

Conversely, an obvious synergistic effect of plasma with the catalyst was measured in the plasma + Ag/ZnO system, showing a dramatic increase in CO_2 conversion to 76.5%, and the selectivity and yield of CO also increased to 96.8% and 74.1%, respectively. The results suggest Ag/ZnO possesses numerous active sites on its surface, which significantly enable RWGS to proceed through surface reactions under the plasma condition. Specifically, the electronic interaction between Ag and ZnO results in the formation of electron-deficient Ag sites (Fig. 2(b)), which can promote the dissociation of H_2 and its migration to the ZnO surface (Fig. 3(a)). At the same time, a large number of Ov and reduced ZnO_x (Figs. 2(c) and 2(d)) can effectively adsorb and dissociate CO_2 and excited-state CO_2 (Fig. 3(b)), and combine with spillover hydrogen or gaseous hydrogen radicals (as illustrated in Fig. S5, cf. ESM), generating CO with high selectivity.

To investigate the influence of Ag loading and support material on plasma-catalytic performance, we systematically synthesized a series of Ag/ZnO catalysts with Ag content varied from 2 to 20 wt % (Fig. S6(a), cf. ESM) and evaluated Ag-based catalysts supported on different materials, including Ag/CeO_2, Ag/SiO_2, and $Ag/\gamma\text{-}Al_2O_3$, respectively, to assess their catalytic behaviors. The plasma-catalytic performance on CO_2 conversion is shown in Figs. S7(a) and S7(b) (cf. ESM), suggesting that the most effective loading of Ag is 5 wt %. The CO_2

conversion of Ag/ZnO is notably superior to that of other silver-based catalysts (Fig. S7(b), cf. ESM), highlighting the favorable EMSI between Ag and ZnO that enhances catalytic activity. Furthermore, we examined the effects of feed gas flow rate (Fig. S7(c), cf. ESM) and discharge voltage (Fig. S7(d), cf. ESM), revealing that CO_2 conversion exhibits a negative correlation with feed gas flow rate and a positive correlation with applied voltage.

Under conditions of optimal Ag loading and discharge voltage, we tested the stability of the plasma-catalytic RWGS over Ag/ZnO (Figs. 4(b) and Fig. S8 (cf. ESM)). The results demonstrate that during a 6 h reaction on stream, CO_2 conversions and CO selectivity remained at ~76.5% and ~96.8%, which is very stable and significantly higher than that of the control systems of plasma alone and plasma + ZnO. The mild plasma condition did not affect the physicochemical properties of Ag/ZnO as evidenced by the comparative pre-/post-reaction characterization, showing the almost unchanged morphology (Fig. S3(c), cf. ESM), surface area (Fig. S4, cf. ESM), phase structure (Fig. S6(b), cf. ESM), and chemical state (Fig. S9, cf. ESM).

The energy efficiency of a plasma-assisted catalytic process is a key parameter for assessing the practical viability of plasma-enabled technology. We calculated the energy efficiency based on CO yield under various reaction conditions. As shown in Fig. 4(c), the RWGS reaction carried out under the conditions of "plasma alone" and "plasma + ZnO" exhibits similar energy efficiency for CO production, which is 0.056 and 0.051 $mmol \cdot kJ^{-1}$, respectively. However, when coupling plasma with Ag/ZnO, the energy efficiency experienced an enhancement to 0.192 $mmol \cdot kJ^{-1}$, outperforming most previous research on plasma catalytic RWGS processes (Fig. S10, cf. ESM) and achieving nearly a 4-fold improvement compared to that of the "plasma alone" and the "plasma + ZnO" conditions. This underscores a significant reduction in energy consumption, highlighting the effectiveness of an appropriate catalyst.

Figure 4(d) compares our results with several representative results from the literature regarding plasma-assisted RWGS reaction using different packing materials or catalysts [3,7,8,11,12,15,22,35]. Notably, CO_2 conversions in most state-of-the-art cases were lower than 50%, while the Ag/ZnO catalysts here demonstrate a superior CO_2 conversion of 76.5%, and its CO selectivity is comparable to the optimal values reported by previous studies.

4 Conclusions

In this study, Ag/ZnO catalysts were prepared and studied for plasma-catalytic RWGS reaction. Remarkable performance was achieved, including a CO_2 conversion of 76.5%, CO selectivity of 96.8%, a CO yield of 74.1%, and an energy efficiency as high as 0.19 $mmol \cdot kJ^{-1}$, with stable operation maintained over 6 h. Catalyst characterization reveals the EMSI between Ag and ZnO, which significantly influences the surface environments of Ag/ZnO and is responsible for the excellent performance in plasma-catalytic CO_2 hydrogenation for CO production. Such EMSI facilitates the formation of electron-deficient Ag sites, enhancing the adsorption and dissociation of H_2. Concurrently, EMSI promotes the creation of coordinatively unsaturated Zn sites (i.e., ZnO_x) and additional Ov after reduction treatment, which further enhances CO_2 adsorption and activation. These surface site modifications provide a dominant plasma-assisted surface reaction pathway over Ag/ZnO for improved CO_2 hydrogenation: the effective hydrogenation of adsorbed CO_2 over the surface of Ag/ZnO by spillover hydrogen or gaseous hydrogen radicals. This work demonstrates the crucial role of EMSI in the rational design of catalysts and highlights the potential of emerging plasma-catalytic processes for CO_2 hydrogenation to CO under ambient conditions using Ag/ZnO catalyst.

Competing interests The authors declare that they have no competing interests.

Acknowledgements The authors acknowledge the financial support from the Natural Science Foundation of Jiangxi Province (Grant No. 20232BAB214018), the Research Projects of Ganjiang Innovation Academy (Grant No. E355F0050) of the Chinese Academy of Sciences, the National Natural Science Foundation of China (Grant No. W2431016), and the research fund of Key Laboratory of Rare Earth, Ganjiang Innovation Academy, Chinese Academy of Sciences.

Electronic Supplementary Material Supplementary material is available in the online version of this article at https://doi.org/10.1007/s11705-025-2588-4 and is accessible for authorized users.

References

1. Ashford B, Poh CK, Ostrikov K, Chen L, Tu X. Plasma-catalytic CO_2 hydrogenation to ethane in a dielectric barrier discharge reactor. Journal of CO_2 Utilization, 2022, 57: 101882
2. Chen H, Mu Y, Shao Y, Sarayute C, Huan X, Jiao Y, Hardacre C, Fan X. Nonthermal plasma (NTP) activated metal-organic

frameworks (MOFs) catalyst for catalytic CO_2 hydrogenation. AIChE Journal, 2020, 66(4): e16853

3. Zeng Y X, Wang L, Wu C F, Wang J Q, Shen B X, Tu X. Low temperature reforming of biogas over K-, Mg-, and Ce-promoted Ni/Al_2O_3 catalysts for the production of hydrogen rich syngas: understanding the plasma-catalytic synergy. Applied Catalysis B: Environmental, 2018, 224: 469–478
4. Zhao T, Hui Y, Li Z. Review of plasma-assisted reactions and potential applications for modification of metal-organic frameworks. Frontiers of Chemical Science and Engineering, 2019, 13(3): 444–457
5. Ashford B, Wang Y, Poh C K, Chen L, Tu X. Plasma-catalytic conversion of CO_2 to CO over binary metal oxide catalysts at low temperatures. Applied Catalysis B: Environment and Energy, 2020, 276(0): 119110
6. Li X, Sen Y, Zhang X. A review on the low temperature water-gas-shift reaction: reaction mechanism, catalyst design, and novel process development. Frontiers of Chemical Science and Engineering, 2025, 19(6): 46
7. Liu M, Yi Y, Wang L, Guo H, Bogaerts A. Hydrogenation of carbon dioxide to value-added chemicals by heterogeneous catalysis and plasma catalysis. Catalysts, 2019, 9(3): 275
8. Kim Y, Kim K J, Song Y, Lee Y L, Roh H S, Na K. Highly CO-selective Ni-MgO-$Ce_xZr_{1-x}O_2$ catalyst for efficient low-temperature reverse water-gas shift reaction. Journal of Industrial and Engineering Chemistry, 2023, 118: 341–350
9. Ussiri D A N, Lal R. Long-term tillage effects on soil carbon storage and carbon dioxide emissions in continuous corn cropping system from an alfisol in Ohio. Soil & Tillage Research, 2009, 104(1): 39–47
10. Zhu X, Liu J H, Li X S, Liu J L, Qu X, Zhu A M. Enhanced effect of plasma on catalytic reduction of CO_2 to CO with hydrogen over Au/CeO_2 at low temperature. Journal of Energy Chemistry, 2017, 26(3): 488–493
11. Liu L, Zhang Z, Das S, Xi S, Kawi S. $LaNiO_3$ as a precursor of Ni/La_2O_3 for reverse water-gas shift in DBD plasma: effect of calcination temperature. Energy Conversion and Management, 2020, 206: 112475
12. Chen H, Mu Y, Shao Y, Sarayute C S, Goodarzi F, Mielby J J, Mao B, Sooknoi T, Hardacre C, Kegnæs S, et al. Effect of metal dispersion and support structure of Ni/silicalite-1 catalysts on non-thermal plasma (NTP) activated CO_2 hydrogenation. Applied Catalysis B: Environmental, 2020, 272: 119013
13. Chen Y, Chen S, Shao Y, Cui Q, Gao N, Fan X, Chen H. Siliceous mesocellular foam supported Cu catalysts for promoting non-thermal plasma activated CO_2 hydrogenation toward methanol synthesis. Frontiers of Chemical Science and Engineering, 2024, 18(7): 77
14. Wang L, Yi Y, Wu C, Guo H, Tu X. One-step reforming of CO_2 and CH_4 into high-value liquid chemicals and fuels at room temperature by plasma-driven catalysis. Angewandte Chemie International Edition, 2017, 56(44): 13679–13683
15. Pastor-Pérez L, Shah M, Le Saché E, Ramirez Reina T. Improving Fe/Al_2O_3 catalysts for the reverse water-gas shift reaction: on the effect of Cs as activity/selectivity promote. Catalysts, 2018, 8(12): 608
16. Xu S, Sarayute C, Shao Y, Xu S, Wang Y C, Haigh S, Mu Y, Jiao Y, Stere C E, Chen H, et al. Mechanistic study of non-thermal plasma assisted CO_2 hydrogenation over Ru supported on MgAl layered double hydroxide. Applied Catalysis B: Environmental, 2020, 268: 118752
17. Liu L, Dai J, Yang Z, Li Y, Su X, Zhang Z. Plasma-catalytic carbon dioxide conversion by reverse water-gas shift over $La_{0.9}Ce_{0.1}B_{0.5}B'_{0.5}O_{3-\delta}$ perovskite-derived bimetallic catalysts. Chemical Engineering Journal, 2022, 431: 134009
18. Sun Y, Wu J, Wang Y, Li J, Wang N, Harding J, Mo S, Chen L, Chen P, Fu M, et al. Plasma-catalytic CO_2 hydrogenation over a Pd/ZnO catalyst: *in situ* probing of gas-phase and surface reactions. JACS Au, 2022, 2(8): 1800–1810
19. Tang C W, Chuang S S C. The effect of reduction of pretreated NiO-ZnO catalysts on the water-gas shift reaction for hydrogen production as studied by *in situ* DRIFTS/MS. International Journal of Hydrogen Energy, 2014, 39(2): 788–797
20. Ahmad S, Hussain A, Mian S A, Rahman G, Ali S, Jang J. Sensing and conversion of carbon dioxide to methanol using Ag-decorated zinc oxide nanocatalyst. Materials Advances, 2024, 5(3): 1119–1129
21. Wen C, Yin A, Dai W L. Recent advances in silver-based heterogeneous catalysts for green chemistry processes. Applied Catalysis: Environment and Energy, 2014, 160–161: 730−741
22. Mori K, Sano T, Kobayashi H, Yamashita H. Surface engineering of a supported PdAg catalyst for hydrogenation of CO_2 to formic acid: elucidating the active Pd atoms in alloy nanoparticles. Journal of the American Chemical Society, 2018, 140(28): 8902–8909
23. Brugnoli L, Pedone A, Menziani M C, Adamo C, Labat F. H_2 dissociation and water evolution on silver-decorated $CeO_2(111)$: a hybrid density functional theory investigation. Journal of Physical Chemistry C, 2019, 123(42): 25668–25679
24. Mohammad A B, Yudanov I V, Lim K H, Neyman K M, Rösch N. Hydrogen activation on silver: a computational study on surface and subsurface oxygen species. Journal of Physical Chemistry C, 2008, 112(5): 1628–1635
25. Sun K, Zhang Z, Shen C, Rui N, Liu C J. The feasibility study of the indium oxide supported silver catalyst for selective hydrogenation of CO_2 to methanol. Green Energy & Environment, 2022, 7(4): 807–817
26. Yi Y, Li S, Cui Z, Hao Y, Zhang Y, Wang L, Liu P, Tu X, Xu X, Guo H, et al. Selective oxidation of CH_4 to CH_3OH through plasma catalysis: insights from catalyst characterization and chemical kinetics modelling. Applied Catalysis B: Environmental, 2021, 296: 120384
27. Hu J, Kim E M, Janik M J, Alexopoulos K. Hydrogen activation and spillover on anatase TiO_2-supported Ag single-atom catalysts. Journal of Physical Chemistry C, 2022, 126(17): 7482–7491
28. Wang B, Zhang Q, He J, Huang F, Li C, Wang M. Co-catalyst-free large ZnO single crystal for high-efficiency piezocatalytic hydrogen evolution from pure water. Journal of Energy Chemistry, 2022, 65: 304–311
29. Silva R L, Franco J A. Raman spectroscopy study of structural disorder degree of ZnO ceramics. Materials Science in Semiconductor Processing, 2020, 119: 105227

30. Wang D X, Summers C J, Wang Z L. Mesoporous single-crystal ZnO nanowires epitaxially sheathed with Zn_2SiO_4. Advanced Materials, 2004, 16(14): 1215–1218
31. Epling W S, Hoflund G B, Salaita G N. Surface characterization study of the thermal decomposition of Ag_2CO_3. Journal of Physical Chemistry B, 1998, 102(12): 2263–2268
32. Klacar S, Grönbeck H. H_2 dissociation over Ag/Al_2O_3: the first step in hydrogen assisted selective catalytic reduction of NO_x. Catalysis Science & Technology, 2013, 3(1): 183–190
33. Gómez H, Rojas R, Patel D, Tabak L A, Lluch J M, Masgrau L. A computational and experimental study of O-glycosylation, catalysis by human UDP-GalNAc polypeptide: GalNAc transferase-T_2. Organic & Biomolecular Chemistry, 2014, 12(17): 2645–2655
34. Dai R, Sun K, Shen R, Fang J, Cheong W C, Zhuang Z, Zhuang Z, Zhang C, Chen C. Direct microenvironment modulation of CO_2 electroreduction: negatively charged Ag sites going beyond catalytic surface reactions. Angewandte Chemie International Edition, 2024, 63(37): e202408580
35. Chen C, Zheng Y, Zhan Y, Lin X, Zheng Q, Wei K. Enhanced Raman scattering and photocatalytic activity of Ag/ZnO heterojunction nanocrystals. Dalton Transactions, 2011, 40(37): 9566–9570
36. Wen T, Liang L, Wang L, Shao Q, Zhang J, Long C. Adjusting Ag^0 on oxygen-deficient Ag/MnO_2 through electronic metal-support interaction to enhance mineralization of toluene in post-plasma catalytic system. Chemical Engineering Journal, 2024, 493: 152572
37. Zhang Z, Wen G, Luo D, Ren B, Zhu Y, Gao R, Dou H, Sun G, Feng M, Bai Z, et al. “Two ships in a bottle” design for Zn-Ag-O catalyst enabling selective and long-lasting CO_2 electroreduction. Journal of the American Chemical Society, 2021, 143(18): 6855–6864
38. Aziz F F A, Timmiati S N, Jalil A A, Rusdan N A, Annuar N H R, Teh L P. Recent innovation on heterogeneous ZnO-based catalysts for enhanced CO_2 hydrogenation. Journal of Environmental Chemical Engineering, 2024, 12(3): 112976
39. Xiao M, Wang L, Wang H, Yuan J, Chen X, Zhang Z, Fu X, Dai W. Oxygen vacancies stabilized Ag^+ to enhance the performance of an Ag/In_2O_3 photocatalyst for non-oxidative coupling of methane. Catalysis Science & Technology, 2023, 13(14): 4148–4155
40. Hu B, Yin Y, Liu G, Chen S, Hong X, Tsang S C E. Hydrogen spillover enabled active Cu sites for methanol synthesis from CO_2 hydrogenation over Pd doped CuZn catalysts. Journal of Catalysis, 2018, 359: 17–26
41. Phongamwong T, Chantaprasertporn U, Witoon T, Numpilai T, Poo-arporn Y, Limphirat W, Donphai W, Dittanet P, Chareonpanich M, Limtrakul J. CO_2 hydrogenation to methanol over CuO-ZnO-ZrO_2-SiO_2 catalysts: effects of SiO_2 contents. Chemical Engineering Journal, 2017, 316: 692–703
42. Li L, Mao D, Yu J, Guo X. Highly selective hydrogenation of CO_2 to methanol over CuO-ZnO-ZrO_2 catalysts prepared by a surfactant-assisted co-precipitation method. Journal of Power Sources, 2015, 279: 394–404
43. Singha R K, Yadav A, Agrawal A, Shukla A, Adak S, Sasaki T, Bal R. Synthesis of highly coke resistant Ni nanoparticles supported MgO/ZnO catalyst for reforming of methane with carbon dioxide. Applied Catalysis B: Environment and Energy, 2016, 191: 165–178
44. Jia X, Zhang X, Rui N, Hu X, Liu C J. Structural effect of Ni/ZrO_2 catalyst on CO_2 methanation with enhanced activity. Applied Catalysis B: Environment and Energy, 2019, 244: 159–169
45. Chen C S, Cheng W H, Lin S S. Study of reverse water gas shift reaction by TPD, TPR, and CO_2 hydrogenation over potassium-promoted Cu/SiO_2 catalyst. Applied Catalysis A: General, 2003, 238(1): 55–67
46. Kast P, Friedrich M, Girgsdies F, Kröhnert J, Teschner D, Lunkenbein T, Behrens M, Schlögl R. Strong metal-support interaction and alloying in Pd/ZnO catalysts for CO oxidation. Catalysis Today, 2016, 260: 21–31
47. Liu L, Das S, Chen T, Dewangan N, Ashok J, Xi S, Borgna A, Li Z, Kawi S. Low temperature catalytic reverse water-gas shift reaction over perovskite catalysts in DBD plasma. Applied Catalysis B: Environment and Energy, 2020, 265: 118573